RSC Advances

ROYAL SOCIETY OF CHEMISTRY

PAPER

View Article Online
View Journal | View Issue

Check for updates

Cite this: *RSC Adv.*, 2025, **15**, 48923

Sustainable incorporation of waste toner derived Fe_3O_4 into reduced graphene oxide for electrochemical dopamine sensing

Sourav Datta,[ac] Md Humayun Kabir, *[b] Md. Shahidur Rahman,[c] Md Yeasin Pabel,[a] Tajnin Jahan,[a] Tasnuva Sharmin[d] and Sabina Yasmin *[a]

Received 13th October 2025
Accepted 28th November 2025

DOI: 10.1039/d5ra07817b

rsc.li/rsc-advances

The improper disposal of electronic waste (e-waste) poses significant environmental challenges but also presents an opportunity for sustainable material recovery. Simultaneously, dopamine (DA) is a vital neurotransmitter involved in numerous physiological processes, and its sensitive detection is essential for diagnosing neurological disorders. In this study, we report a cost-effective and environmentally friendly strategy to synthesize a reduced graphene oxide–magnetite (rGO–Fe_3O_4) nanocomposite from e-waste-derived precursors for DA sensing. Graphite was recovered from spent lithium-ion battery (LIB) anodes *via* ultrasonication, while Fe_2O_3 was obtained from waste toner powder (WTP) through thermal decomposition. Graphene oxide (GO) was synthesized from the purified graphite using an improved Hummers' method and subsequently reduced in the presence of Fe_2O_3 to form the rGO–Fe_3O_4 nanocomposite. The resulting materials were characterized by FTIR, SEM-EDS, and XRD analyses. The rGO–Fe_3O_4-modified glassy carbon electrode (GCE) exhibited excellent electrocatalytic performance for DA detection, as evaluated by cyclic voltammetry (CV), differential pulse voltammetry (DPV), and amperometry. The sensor demonstrated a wide linear detection range (10–450 μM), high sensitivity (42.35 μA mM^{-1}), and a low detection limit (0.0639 μM). It also showed outstanding selectivity, repeatability, and stability, along with successful DA quantification in human urine samples. This work presents a circular materials approach for converting e-waste into functional nanocomposites and underscores their potential in the development of affordable, high-performance electrochemical biosensors.

1. Introduction

Rapid urbanization and industrialization in the past few decades have increased the demand for electrical and electronic appliances in both household and office settings. As a consequence of the increasing usage of these devices, a concerning amount of "e-waste" is being produced. The production of e-waste in the years 2016, 2019, and 2022 was 44.7, 53.6, and 62 million metric tons, respectively, according to the Global E-waste Monitor.[1–3] Printer cartridges are a significant source of e-waste. About a million cartridges are cast off daily worldwide.[4] Printer cartridges contain toner powder which is composed of Fe_3O_4, SiO_2, carbon, and styrene-acrylate copolymer.[5] About 8% toner powder by weight remains unused from each cartridge which is subsequently responsible for the ejection of ∼6000 tons of carbon powder in the environment.[6,7] Additionally, about 2500 tons of iron waste originated from waste toner powder (WTP) is released in the landfill sites annually.[8] Thus, the disposal of WTP in outdoors and *via* landfilling pollutes soil, air, and water. Moreover, due to potential risk of ignition and combustion, WTP has been included as a hazardous waste.[9]

On the context of e-waste, spent batteries are one of the major contributors. Especially, exhausted lithium ion batteries (LIBs) can have menacing impact on environment and human health due to their hazardous components like Li, Co, Ni, organic electrolytes *etc.*[10,11] Also, the possibility of ignition and explosion due to mismanagement of discarded LIBs with residual charge adds to a crucial risk factor.[12] The annual projected amount of 14 million waste LIBs by 2040 increases more concern regarding this situation.[13]

Therefore, a well-planned, legitimate, and useful recycling of both WTP and LIBs will directly aid in the preservation of our atmosphere as well as human health. Some research works have been reported on reusing WTP materials such as for organic dye extracting adsorbent, removal of Cr(VI), sodium battery material

---

[a] Institute of National Analytical Research and Service (INARS), Bangladesh Council of Scientific and Industrial Research (BCSIR), Dhanmondi, Dhaka-1205, Bangladesh. E-mail: sabinayasmin@bcsir.gov.bd

[b] Institute of Food Science and Technology (IFST), Bangladesh Council of Scientific and Industrial Research (BCSIR), Dhanmondi, Dhaka-1205, Bangladesh. E-mail: humayunkabir@bcsir.gov.bd

[c] Department of Chemistry, University of Dhaka, Dhaka-1000, Bangladesh

[d] Department of Pharmaceutical Chemistry, University of Dhaka, Dhaka-1000, Bangladesh

designing and so on.[14–16] Besides, consumed LIBs have been recycled to obtain pure metals and their oxides.[17] Also, the waste graphite powder content can be used to prepare useful derivatives (*e.g.* exfoliated graphite, graphene oxide *etc.*) which find their use in electrochemical sensing,[18] antibiotic removal,[19] organic dye adsorption,[20] designing supercapacitors[21] *etc.* The current work utilises both WTP and LIBs as the raw materials of our synthesized nanocomposite used in electrochemical sensing of dopamine.

Dopamine (DA), known otherwise as 3,4-dihydroxyphenethylamine is a neuromodulatory molecule which plays a pivotal role in the function of cardiovascular, central nervous, hormonal, and renal system. DA regulates many physiological states like mood, behaviour, memory, attention, perception, learning, reasoning, motor control and so on.[22] Deficiency of DA in human body can trigger neurological abnormalities such as attention deficit hyperactivity disorder (ADHD), Parkinson's disease, restless leg syndrome *etc.*[23–25] Then again, excess concentration of DA leads to schizophrenia, addiction, and cardiotoxicities.[26,27] Therefore, dopamine assessment is a crucial factor in the early diagnosis of these medical conditions.

Diverse analytical methods, such as chemiluminescence, spectrophotometry, high performance liquid chromatography, fluorescence, colorimetry and so forth have been employed for measuring DA.[28–30] Being an electro-active compound, DA can be sensed electrochemically. The electrochemical assessment approach is preferable due to its robustness, convenient and fast operation, low-cost, low detection limit, high sensitivity and selectivity.

Graphene and its derivatives have been extensively utilized in the domain of electrochemical detection.[31,32] Graphene oxide (GO) is one such derivative which has high surface area and reactivity that allows smooth compositing with desired metal or metal oxides. In addition, good electrical characteristics make GO an ideal supporting material pertaining to electrochemical evaluation.[33] However, pure GO is costly. To address this problem, electronic waste can come in handy. Spent LIBs contain a copper foil coated with graphite. This graphite content can be used to prepare inexpensive GO following improved Hummers' method. GO synthesis in such way is not only cost effective but also ensures efficient reprocessing of the discarded LIBs.

Reduced graphene oxide (rGO) is preferred over GO in sensing work due to the higher electrical conductivity of rGO and more ease in fabrication. Nevertheless, both GO and rGO supported metal oxide nanomaterials have been widely prepared to use as DA sensors.[34,35] Specifically, Fe_3O_4, also known as magnetite or magnetic iron oxide is highly conductive, stable, non-toxic, and biocompatible. Moreover, the significant catalytic dynamism of Fe_3O_4 nanoparticles (NPs) has made them immensely effective in electrochemical assessment.[36,37]

In recent years, converting waste streams into functional electrode materials for electrochemical sensing has attracted significant attention. Waste-derived reduced graphene oxide (rGO) has been explored as a high-surface-area conductive platform for detecting biologically and environmentally relevant analytes.[18,38,39] Meanwhile, although still limited, a few waste-sourced composites of Fe_3O_4 have been prepared and applied for electrochemical sensing.[40,41]

Compared with these single-waste strategies, the present study converts two abundant and underutilized waste materials, discarded LIBs and WTP into a functional nanocomposite *via* simple chemical-reduction process, demonstrating an efficient dual-waste valorization strategy for sensor fabrication. Graphite recovered from LIB anodes was used to synthesize GO, which was chemically reduced to rGO, while ferric oxide derived from thermally treated WTP served as the precursor for Fe_3O_4 nanoparticles. These waste-derived components were integrated into an rGO–Fe_3O_4 nanocomposite and fabricated onto a glassy carbon electrode (GCE) to produce a low-cost, high-performance DA sensor. Comprehensive physicochemical characterization confirmed the successful formation and chemical integration of the hybrid nanostructure. Electrochemical analyses using cyclic voltammetry, differential pulse voltammetry, and amperometry revealed high sensitivity, a low detection limit, and excellent selectivity for DA, even in real biological samples.

Beyond its electroanalytical performance, this work establishes a compelling precedent for circular materials chemistry, upcycling hazardous electronic waste into value-added functional nanomaterials with real-world biomedical sensing applications. The dual recovery and integration of carbonaceous and metal oxide phases from distinct waste streams into a unified sensing interface represents a rare, eco-conscious innovation with practical impact.

2. Experimental

2.1 Reagents and chemicals

Dopamine hydrochloride ($(HO)_2C_6H_3CH_2CH_2NH_2 \cdot HCl$) (CAS No. 62-31-7), sodium phosphate monobasic dihydrate ($NaH_2PO_4 \cdot 2H_2O$) (CAS No. 13472-35-0), 4-nitrophenol ($O_2NC_6H_4OH$) (CAS No. 100-02-7), and D-(+)-glucose ($C_6H_{12}O_6$) (CAS No. 50-99-7) were purchased from Sigma-Aldrich (Merck), Germany. Sulfuric acid (H_2SO_4) (95–97%, CAS No. 7664-93-9) and potassium permanganate ($KMnO_4$) (CAS No. 7722-64-7) were purchased from Scharlau, Spain. Serotonin hydrochloride ($C_{10}H_{12}N_2O \cdot HCl$) (CAS No. 153-98-0), sodium hydroxide (NaOH) (CAS No. 1310-73-2), hydrochloric acid (HCl) (37%, CAS No. 7647-01-0), and hydrogen peroxide (H_2O_2) (30%, CAS No. 7722-84-1) were purchased from Sigma-Aldrich, USA. Sodium phosphate dibasic heptahydrate ($Na_2HPO_4 \cdot 7H_2O$) (CAS No. 7782-85-6) was purchased from Sigma-Aldrich, India. Uric acid ($C_5H_4N_4O_3$) (CAS No. 69-93-2) was purchased from Sigma-Aldrich, Switzerland. Phosphoric acid (H_3PO_4) (85%, CAS No. 7664-38-2) was purchased from Janssen Chemica, Belgium. Ethanol (C_2H_5OH) (98%, CAS No. 64-17-5) was purchased from AppliChem, Germany. Hydrazine hydrate ($N_2H_4 \cdot H_2O$) (80%, CAS No. 7803-57-8) was purchased from Finar Limited, India. All reagents were of analytical grade and utilized without further purification. Necessary solutions were prepared using ultrapure deionized water having a resistivity of 18 MΩ cm at room temperature.

2.2 Instrumental characterization

Electrochemical assessments were carried out by CHI660 device (USA) with a glassy carbon electrode (CHI104, $\Phi = 3$ mm), Ag/AgCl/KCl (saturated) (CHI111) reference electrode, and a counter electrode of spiral platinum wire (BAS Inc., 23 cm). Surface characterization of the prepared samples was performed utilizing scanning electron microscopy (SEM) (Zeiss EVO18, Germany) at different magnifications using a 15 kV electron beam voltage. Energy dispersive X-ray spectroscopy (EDS) (TEAM EDS; EDAX, USA) was employed in deduction of elemental composition. For acquiring detailed morphological features of the prepared nanocomposite, transmission electron microscopy (TEM) (Talos F200X, Thermo Fisher Scientific, USA) with an accelerating voltage of 200 kV was employed. Fourier transform infrared (FTIR) spectra were recorded using a Fourier transform spectrophotometer (IRPrestige-21, SHIMADZU, Japan), in transmittance mode. The X-ray diffraction (XRD) patterns of the synthesized materials were obtained using an X-ray diffractometer (Ultima IV, Rigaku, Japan) equipped with a Cu K$\alpha_1 = 1.5406$ Å source and running at 40 kV–30 mA with an exposure time of 20 minutes.

2.3 Recovery of graphite from Li-ion battery

Graphite powder was acquired from spent Li-ion batteries. Firstly, the shells and other wrappers of the batteries were peeled off with the assistance of a plier. The anode and cathode materials were separated cautiously. Anode is composed of graphite coated copper foil. These foils were then immersed in DI water in a beaker and ultrasonicated for an hour. In such manner, the graphite coating was segregated from the copper foils. The graphite content was filtered and then treated with aqua regia for the removal of any inorganic impurities followed by further washing with DI water. Finally, it was dried in an oven at 60 °C for 24 hours.

2.4 Conversion of waste toner powder to ferric oxide

Waste toner powder was extracted from printer cartridges available in offices and marketplaces. At first, cartridges were separated carefully from printers using mechanical tools. Then, the toner hoppers were detached from their cartridges to extract the toner powder. The WTP was collected in a porcelain crucible and initially heated at 150 °C temperature in a muffle furnace. The temperature was increased by 50 °C every 30 minutes until it reached 600 °C. Finally, the sample was decomposed at 600 °C for 2 hours and the end product obtained was brick red-colored Fe_2O_3, as confirmed by FTIR and XRD analyses (discussed later). Thermal processing of 17.08 g WTP produced 7.86 g of ferric oxide, corresponding to a ~46% yield based on the mass of the waste precursor.

2.5 Synthesis of GO

An improved Hummers' method was applied to prepare GO from the graphite powder derived from LIBs.[42] In short, in an acid mixture of H_2SO_4 and H_3PO_4 (9 : 1), graphite powder and $KMnO_4$ were added with continuous stirring. Then the reaction mixture was heated for 12 hours at 50 °C. The mixture was then allowed to cool at room temperature and placed in an ice bath to reduce the temperature to as low as 4 °C. H_2O_2 (30%) and DI water were added slowly in the mixture with constant stirring to remove excess $KMnO_4$. The product thus obtained was separated by centrifugation followed by washing with HCl (30%). The product was again washed with DI water until the point of neutralization and finally treated with absolute ethanol for the removal of any organic impurities. Acquired GO was dried in an oven for 24 hours at 60 °C. The chemical oxidation of 3 g of graphite yielded 3.78 g of GO, corresponding to a 26% mass increase due to the incorporation of oxygen functionalities during oxidation.

2.6 Synthesis of rGO–Fe_3O_4

A dispersion of 100 mg GO in 100 mL DI water was prepared in a round bottom flask by means of ultrasonication. 25 mg of Fe_2O_3 was digested by HCl (37%) and put into the GO dispersion. The pH of the mixture was controlled to 7. After the addition of 1 mL hydrazine hydrate, the mixture was refluxed at 120 °C for 3 hours. Post-reflux, the mixture exhibited a pH of 10. The product was isolated by centrifugation and washed repeatedly with DI water and lastly by absolute ethanol to remove impurities. The product was then dried under vacuum condition at 60 °C for 24 hours. The synthesis procedure of rGO follows the identical pathway as rGO–Fe_3O_4 except the addition of iron content.

2.7 Fabrication of rGO–Fe_3O_4 modified GCE

The GCE was carefully polished using an aqueous slurry of alumina powder (0.05 μm) on a micro cloth polishing pad. The electrode was then thoroughly rinsed with deionized (DI) water to ensure the removal of any physically adsorbed particles from the surface. To modify the GCE, a suspension of rGO–Fe_3O_4 in DI water (1 mg mL^{-1}) was prepared by sonicating the mixture for 30 minutes. Precisely, 8 μL of the homogenous suspension was meticulously drop cast onto the bare, polished GCE and air-dried at room temperature to obtain a uniform active material film of 0.1 mg cm^{-2}.

2.8 Electrochemical measurements

All electrochemical measurements were performed in 0.1 M phosphate buffer solution (PBS, pH 7.4) as the supporting electrolyte. Prior to each experiment, the electrolyte was purged with Ar for 15 minutes. For pH-dependent studies, PBS with the desired pH values (3–10) were prepared. Cyclic voltammetry (CV) was carried out typically at a scan rate of 50 mV s^{-1} within a potential window of −0.1 to 0.6 V *vs.* Ag/AgCl/KCl (sat.). Scan-rate-dependent CVs were additionally recorded by varying the scan rate (10–400 mV s^{-1}). Differential pulse voltammetry (DPV) measurements were performed using a potential increment of 4 mV, pulse amplitude of 50 mV, pulse width of 60 ms, and pulse period of 0.5 s. The DPV potential window was −0.1 to 0.5 V *vs.* Ag/AgCl/KCl (sat.). Amperometric experiments were conducted by applying a constant potential of 0.15 V.

3. Results and discussion

3.1 Synthesis and characterization

3.1.1 Morphological and elemental analysis. The microstructure of both rGO and rGO–Fe_3O_4 nanocomposite were investigated through SEM analysis which revealed valuable insights into the morphology of the materials. Fig. 1a displays sheet-like structure of rGO adorned with prominent folds, wrinkles, and crumples.[39] Such features increase the effective surface area, thus offering more active sites for adsorption and enhancing efficient electrochemical interactions. The SEM image of rGO–Fe_3O_4 (Fig. 1b) shows that the Fe_3O_4 network is anchored onto the surface of the rGO layer and closely resembles with previously reported literature.[43] The elemental composition of the nanocomposite was elucidated by EDS spectrum as shown in Fig. 1c, where C, O, and Fe were found to be the primary elements with the weight percentage of 51.40, 30.92, and 17.68%, respectively. The results demonstrate successful incorporation of Fe_3O_4 into the rGO matrix.

TEM analysis was performed for a more comprehensive view of the nanomorphology of rGO–Fe_3O_4, as shown in Fig. 1d–f. The TEM images show some distinct distorted spherical shaped particles along with some degree of agglomeration. Fig. 1e displays the presence of numerous pores within the framework of Fe_3O_4 attached to rGO layer. These pores should contribute to the amount of active adsorption centers, thereby amplifying the electrochemical performance. The average particle diameter was approximated as 18.77 nm by ImageJ software (64 bit). Moreover, the selected area electron diffraction (SAED) pattern (Fig. 1f) reveals evident diffraction rings from which the interplanar spacings of the nanomaterial's lattice planes were determined. These d-spacings obtained from SAED rings are in good agreement with those measured from XRD data and the apparent diffraction rings correspond to (220), (311), (400), (440), and (533) lattice planes of Fe_3O_4.

3.1.2 FTIR analysis. Functional groups of the synthesized compounds were characterized by FTIR spectra, which provided detailed insight into the stepwise chemical transformations leading to the formation of the rGO–Fe_3O_4 nanocomposite as presented in Fig. 2a. GO shows a broad peak around 3440 cm^{-1} which can be attributed to O–H stretching of hydroxyl groups present in basal plane, carboxyl groups present in the sheet edges, and adsorbed water molecules.[44,45] The peaks observed at 2927 and 2850 cm^{-1} can be assigned to asymmetric and symmetric stretching of methylene ($-CH_2-$) groups, whereas, the peaks spotted at 1720 and 1631 cm^{-1} are attributed to C=O and aromatic C=C stretching of GO, respectively. Moreover, the peaks at 1400, 1226 and 1087 cm^{-1} may be ascribed to O–H bending, C–O stretching of epoxy groups, and C–O stretching of alkoxy groups, respectively.[38,46] These features confirm a highly functionalized carbon surface with diverse oxygenated moieties. Upon chemical reduction to rGO, these oxygen-related bands

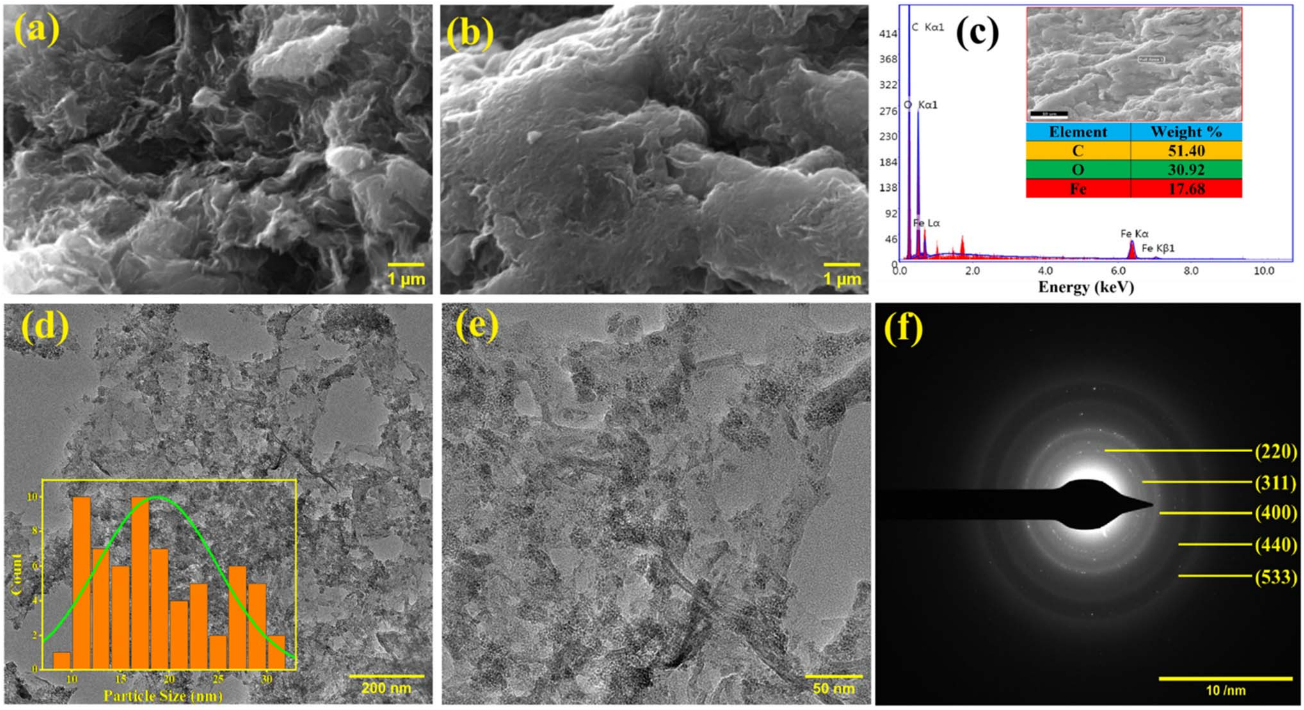

Element	Weight %
C	51.40
O	30.92
Fe	17.68

Fig. 1 SEM images of (a) rGO and (b) rGO–Fe_3O_4. (c) EDS spectrum of rGO–Fe_3O_4, with the inset displaying full analyzed area (top) and elemental composition (bottom). (d and e) TEM images of rGO–Fe_3O_4 at two different magnifications, with the inset of (d) showing the particle size distribution histogram. (f) SAED pattern of rGO–Fe_3O_4.

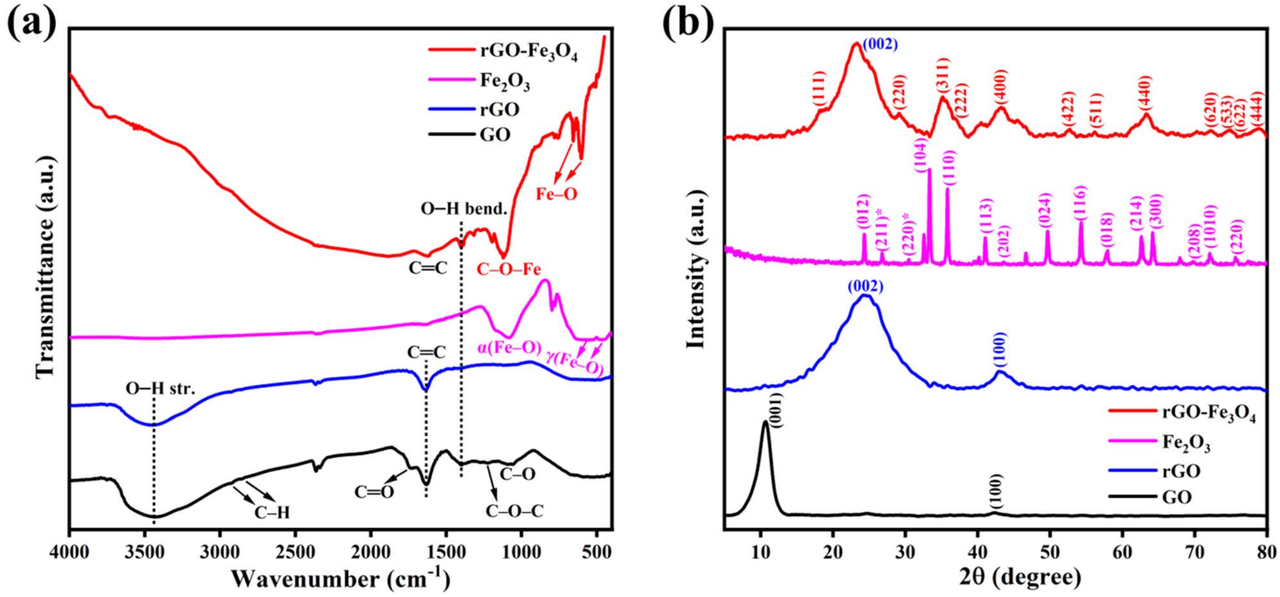

Fig. 2 (a) FTIR spectra (str. = stretching, bend. = bending) and (b) XRD patterns of GO, rGO, Fe_2O_3, and rGO–Fe_3O_4 (* indicates the lattice planes corresponding to γ-Fe_2O_3).

are significantly attenuated as shown in Fig. 2a. The peak intensity for O–H stretching significantly reduced in rGO, whereas this peak completely disappeared in rGO–Fe_3O_4 nanocomposite, which supports removal of hydroxyl groups, typically *via* condensation or hydrazine-mediated reduction. The C═O and epoxy peaks are largely suppressed, indicating decarboxylation and ring-opening reduction reactions, respectively. Together, these spectral changes are consistent with a chemical reduction pathway that re-establishes graphitic conductivity while retaining limited surface functionality. In addition, the prominently sharp aromatic C═C stretching peak observed at both GO and rGO encountered a drastic reduction in intensity in rGO–Fe_3O_4, possibly due to intercalation of Fe_3O_4 NPs between the rGO layers.

The Fe_2O_3 spectrum shows distinctive Fe–O stretching vibration characteristic of the hematite (α-Fe_2O_3) and maghemite (γ-Fe_2O_3) phase which is consistent with the XRD analyses (discussed later). The iron content obtained from WTP displayed an intense peak at 1083 cm^{-1} and comparatively two broader peaks at 574 and 466 cm^{-1}. The former peak is indicative of Fe–O vibration of α-Fe_2O_3, while the latter peaks correspond to the stretching and bending vibration of Fe–O bond present in γ-Fe_2O_3.[5,7] On the other hand, the rGO–Fe_3O_4 showed couple of distinct peaks at 604 and 656 cm^{-1} which may be assigned to Fe–O vibration of Fe_3O_4.[47–49] The band appears slightly shifted and less well-defined compared to pure Fe_3O_4, which is indicative of a modified local bonding environment around the Fe centers suggesting Fe from Fe_3O_4 interact with some oxygen-containing functional groups on rGO. Also, the sharp peak at 1122 cm^{-1} could be due to C–O–Fe stretching vibration which was found at a higher wavenumber than the usual C–O vibration of alkoxy groups of GO and rGO. These observations imply that the Fe_3O_4 nanoparticles are not merely physically adsorbed as evidenced from SEM and TEM images (Fig. 1) but are chemically anchored to the rGO surface.

3.1.3 X-ray diffraction. The XRD patterns shown in Fig. 2b provide structural comparison of the precursors and the nanocomposite and are consistent with the FTIR findings. The sharp diffraction peak observed at $2\theta = 10.6°$ in GO corresponds to the (001) lattice plane, indicating an expanded interlayer spacing due to intercalated oxygen-containing functional groups such as carboxyl, hydroxyl, and epoxy.[38,46] The disappearance of this peak in both rGO and the rGO–Fe_3O_4 nanocomposite confirms the effective chemical reduction of GO, which eliminates interlayer functional groups and collapses the stacked sheets into a more compact structure. This reduction is further supported by the emergence of a broad peak at 23.42° in the nanocomposite, corresponding to the (002) plane of rGO, which is slightly shifted from that of pure rGO (24.48°).[39] The downshift implies structural perturbation of the rGO lattice due to the incorporation of Fe_3O_4 nanoparticles, consistent with probable interfacial C–O–Fe interactions inferred from FTIR (Fig. 2a), which are further discussed in Section 3.1.4. Another evident diffraction peak shown by GO appeared at 42.4° which is characteristic of the turbostratic disorder shown by the material.[50] The WTP-derived iron oxide shows multiple sharp peaks consistent with both α-Fe_2O_3 and γ-Fe_2O_3 phases, reflecting its origin from mixed-valence iron pigments and the oxidative transformation pathway during high-temperature treatment. These species act as a source of Fe^{3+} ions, which, under reduction with hydrazine and controlled pH, participate in the formation of Fe_3O_4 through partial reduction and coprecipitation with Fe^{2+}. WTP derived Fe_2O_3 showed peaks at 24.3, 33.32, 35.8, 40.98, 43.54, 49.74, 54.24, 57.84, 62.66, 64.24, 69.76, 72.14, 75.68° which can be attributed to (012), (104), (110), (113), (202), (024), (116), (018), (214), (300), (208), (1010),

(220) planes of α-Fe_2O_3 respectively, while peaks found at 26.72 and 30.38° align with (211) and (220) planes of γ phase of Fe_2O_3.[7,51,52]

On the other hand, the XRD pattern of the rGO–Fe_3O_4 nanocomposite exhibits distinct peaks of Fe_3O_4 at 29.4, 35.24, 52.74, 56.22, 63.46, 72.24, 74.8, 78.98° which may be assigned to (220), (311), (422), (511), (440), (620), (533), (444) planes and the shoulders at 18.22, 36.8, and 75.42° could correspond to (111), (222), and (622) planes of cubic Fe_3O_4.[8,43,53] Interestingly, both rGO and Fe_3O_4 have one of their signature peaks around 43°. Such characteristic peak has been observed at 43.34° in rGO–Fe_3O_4, which appeared to be broader compared to the pure rGO and likely results from overlapping contributions of the (100) plane of rGO and the (400) plane of Fe_3O_4. This broadening supports the structural coupling between the graphitic layers and the magnetite phase, reinforcing the interfacial interaction. Therefore, the oxygen bridges mediate electron delocalization across the magnetite–carbon interface, enhancing structural integration and facilitating charge transfer for electrochemical DA sensing (see electrochemical performance).

3.1.4 Synthesis mechanism. The synthesis of the rGO–Fe_3O_4 nanocomposite involves a coordinated sequence of redox and complexation reactions that transform e-waste-derived precursors into a functional nanocomposite (Scheme 1). WTP was subjected to thermal oxidation in air at 600 °C. At such elevated temperature, the organic polymers within WTP undergo complete combustion of their carbonaceous matrix and Fe_3O_4 is oxidized by oxygen to form Fe_2O_3 (eqn (1)).[54]

$$2Fe_3O_4 + \tfrac{1}{2}O_2 \rightarrow 3Fe_2O_3 \quad (1)$$

Fe_2O_3 recovered from the thermally treated toner powder is solubilized in concentrated HCl (37%), yielding Fe^{3+} ions *via* the following reaction (eqn (2)).

$$Fe_2O_3 + 6HCl \rightarrow 2FeCl_3 + 3H_2O \quad (2)$$

These Fe^{3+} species, when merely introduced or continuously stirred in an aqueous dispersion of GO, can interact with the oxygen-containing functional groups (–COOH, –OH, epoxides) on GO *via* coordination bonds and electrostatic interactions as evidenced from FTIR and XRD (Sections 3.1.2 and 3.1.3).[55,56] Upon adjusting the pH to neutral condition (pH = 7), partial hydrolysis of free Fe^{3+} may occur (eqn (3)).

$$Fe^{3+} + 3H_2O \rightleftharpoons Fe(OH)_3 + 3H^+ \quad (3)$$

Meanwhile, as a Lewis base, hydrazine readily deprotonates water molecules, producing hydroxide ions (eqn (4)). This phenomenon is clearly manifested by the distinctly alkaline nature of the reaction mixture observed after reflux (see Section 2.6).

$$N_2H_4 + H_2O \rightarrow N_2H_5^+ + OH^- \quad (4)$$

The addition of reducing agent ($N_2H_4 \cdot H_2O$) can initiate a dual redox process: it reduces GO to rGO by eliminating oxygenated groups and restoring sp^2 conjugation (C=O → CH_2; epoxides → C–C) (see Sections 3.1.2 and 3.1.3), while concurrently reducing Fe^{3+} to Fe^{2+} (eqn (5)).

$$4Fe^{3+} + N_2H_5^+ \rightarrow 4Fe^{2+} + N_2 + 5H^+ \quad (5)$$

The coexistence of Fe^{2+} and Fe^{3+} under basic condition drives the coprecipitation of Fe_3O_4 (eqn (6)) as clearly shown in XRD pattern of rGO–Fe_3O_4 (see Section 3.1.3).

$$Fe^{2+} + 2Fe^{3+} + 8OH^- \rightarrow Fe_3O_4 + 4H_2O \quad (6)$$

Simultaneously, GO acts as both a reductive scaffold and a structural template, with surface –OH and $–COO^-$ groups anchoring the growing Fe_3O_4 nanoparticles *via* C–O–Fe linkages (see FTIR and XRD discussion). The π-conjugated surface of rGO may facilitate electron delocalization and provides conductive pathways, while the interfacial coupling between Fe_3O_4 and rGO enhances charge separation and dispersion stability, yielding a chemically integrated, redox-active nanocomposite tailored for electrochemical applications (discussed later).

Compared to the conventional routes for fabricating electrochemical sensors, the present waste-derived synthesis significantly reduces both energy input and material cost. Traditional methods typically require multi-step oxidation/reduction protocols, high-temperature thermal treatments, and commercial precursors, all of which contribute to high energy demand and synthesis expense. In contrast, our

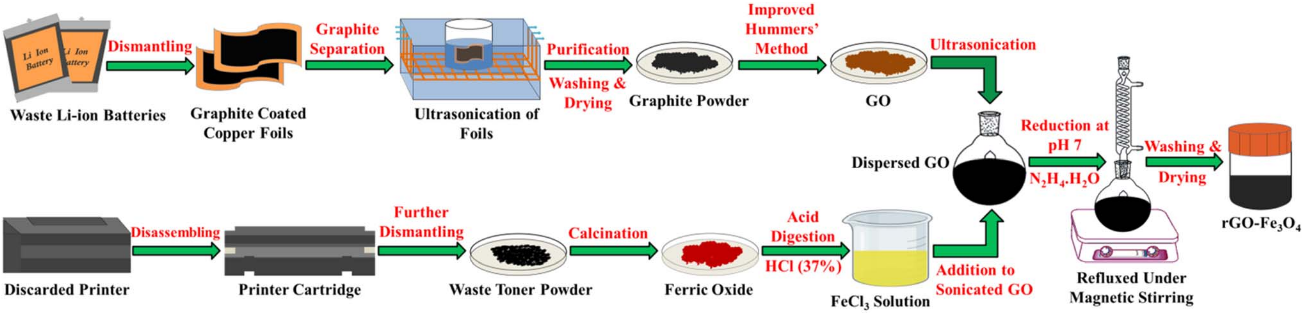

Scheme 1 Synthesis of rGO–Fe_3O_4 nanocomposite utilizing spent Li-ion batteries and waste toner powder.

upcycled approach proceeds at lower temperatures using readily available waste-derived graphene and iron oxide precursors, avoiding both energy-intensive steps and costly reagents. This streamlined process, carried out under mild conditions, therefore represents an economically and environmentally favorable alternative to standard sensor fabrication practices. Furthermore, the protocol is conceptually amenable to industrial-scale e-waste processing, as process-stream management and reagent recovery strategies, along with potential adaptation to continuous or flow-based operations, can enhance efficiency and reduce operational costs during scale-up.

3.2 Electrochemical evaluation of DA on rGO–Fe_3O_4/GCE

3.2.1 Cyclic voltammetry analysis. The electrochemical performance of GCE decorated with rGO–Fe_3O_4 was evaluated and compared with bare GCE, GO/GCE, and rGO/GCE by cyclic voltammetry (CV) technique, as shown in Fig. 3a. These experiments were carried out in Ar-saturated 0.1 M phosphate buffer solution (PBS, pH 7.4) containing 100 μM DA, at 50 mV s^{-1} scan rate. Each electrode showed two distinct peaks, which are associated with the oxidation of dopamine (DA) to dopamine quinone (DAQ) and the subsequent reduction of DAQ to DA, corresponding to the forward and backward scan respectively. Among the electrodes assessed, the rGO–Fe_3O_4/GCE exhibited the most prominent electrochemical response, with an oxidation peak current density of 194.91 μA cm^{-2} at a potential of 0.187 V. This current density exceeded the responses observed for the other electrodes, showing approximately 9.0- and 2.5-times higher response compared to the bare GCE and rGO/GCE, respectively. This improvement is associated with the larger surface area provided by rGO–Fe_3O_4 along with the structural porosity imparted by the Fe_3O_4 NPs as distinctly revealed by the TEM images (see Fig. 1e) which facilitates greater accumulation of DA molecules. The porous Fe_3O_4 NPs provide an enhanced conductive pathway for proton-electron transfer where, Fe(III) oxidizes DA to DAQ and subsequently Fe(II) reduces DAQ to DA on the electro-responsive site of the nanocomposite.[34] For the rGO–Fe_3O_4 electrode, the anodic to cathodic peak current ratio (i_{pa}/i_{pc}) was found to be 1.64 and the voltage separation (ΔE_p)

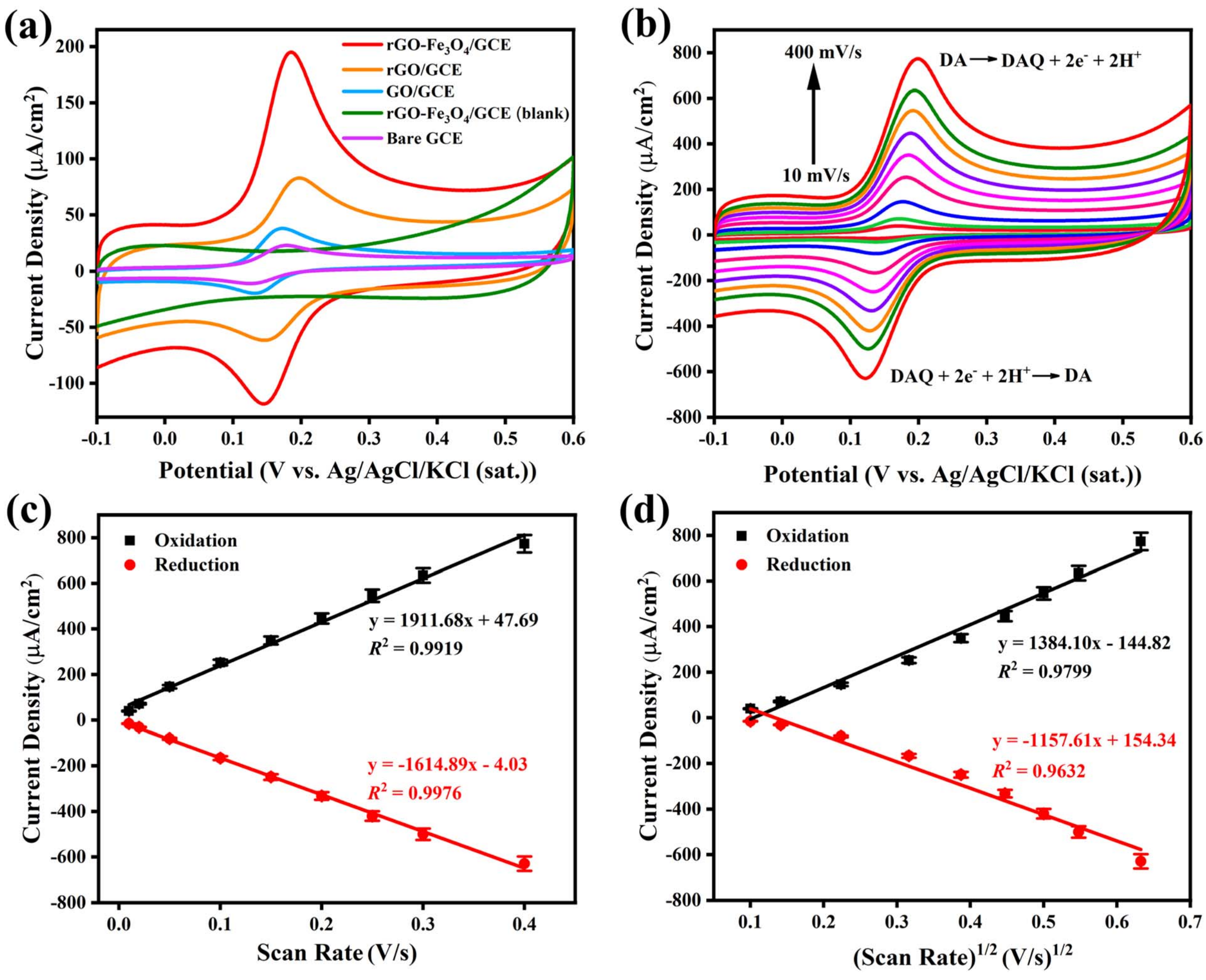

Fig. 3 (a) CVs of bare GCE, GO/GCE, rGO/GCE and rGO–Fe_3O_4/GCE in 0.1 M PBS (pH 7.4) containing 100 μM DA, along with CV of rGO–Fe_3O_4 in blank PBS, where all CVs were performed at 50 mV s^{-1} scan rate. (b) CVs of rGO–Fe_3O_4 coated GCE recorded at scan rate range of 10–400 mV s^{-1} in 0.1 M PBS (pH 7.4) containing 100 μM DA. Plot of redox peak current density *vs.* (c) scan rate and (d) (scan rate)$^{1/2}$.

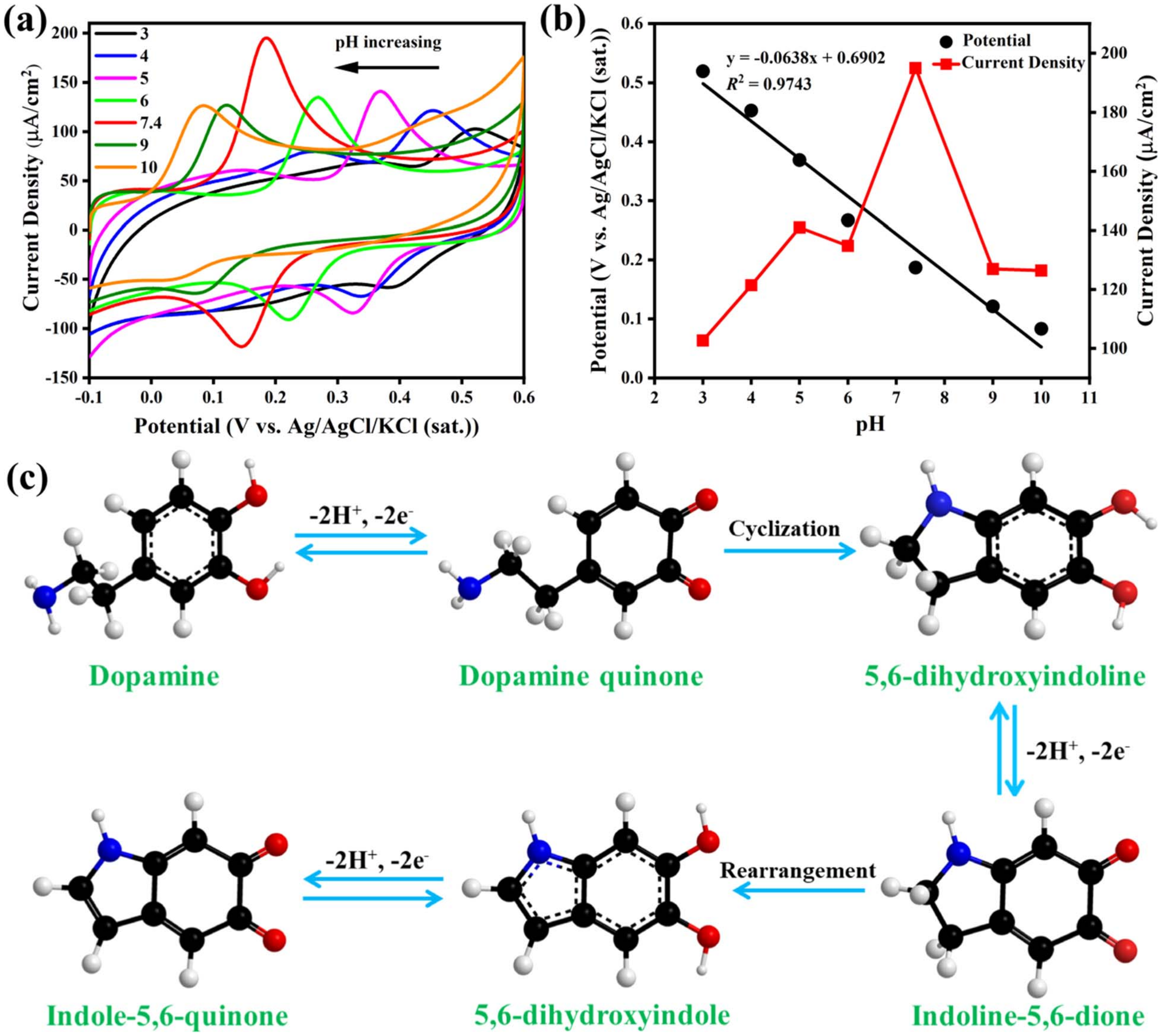

Fig. 4 (a) CVs of rGO–Fe_3O_4/GCE recorded at pH range of 3–10 in 0.1 M PBS containing 100 μM DA at 50 mV s^{-1} scan rate. (b) Plot of oxidation peak current density and peak potential as a function of pH. (c) Proposed electrochemical oxidation mechanism of DA on rGO–Fe_3O_4/GCE in PBS of pH 7.4. (Black, white, blue, and red spheres represent C, H, N, and O atoms, respectively.)

between the current peaks was 41 mV. For a reversible electrochemical reaction, the ideal value of i_{pa}/i_{pc} should be around 1 and that of ΔE_p is expected to be near 30 mV (two electrons transfer).[57,58] The reasonably greater experimental values of these parameters suggest that the redox reaction of DA complies with quasi-reversibility which is in agreement with earlier findings.[33]

3.2.2 Effect of scan rate. Fig. 3b shows CVs for DA redox reaction in 0.1 M PBS (pH 7.4) containing 100 μM DA on rGO–Fe_3O_4/GCE, where the scan rate was varied from 10 to 400 mV s^{-1}. With the increasing scan rate, the current response also increased because at a higher scan rate, potential is swept more rapidly, thus reducing the time available for the analyte species to diffuse. Moreover, diffusion layer thickness (δ) is proportional to the square root of diffusion time and hence δ decreases with increasing scan rate.[59] With the decline of diffusion layer thickness, both faradic and non-faradic current contribution in a CV increase which leads to higher current output. Again, as the scan rate was increased, the oxidation and reduction peak potential gradually shifted towards positive and negative potential values respectively, indicating that at faster scan rates, electron transfer process gets slower.[60]

Changes in current response with variation in scan rate can be fruitful to determine whether the redox reaction of DA is diffusion controlled or adsorption controlled. If oxidation and reduction peak current density (j_{pa} and j_{pc} respectively) are proportional to scan rate (ν), then the process should be adsorption controlled.[61] However, if j_{pa} and j_{pc} exhibit linear relation with $\nu^{1/2}$, the process would be diffusion controlled.[62] Fig. 3c shows regression equations, $j_{pa} = 1911.68\nu + 47.69$ ($R^2 = 0.9919$) and $j_{pc} = -1614.89\nu - 4.03$ ($R^2 = 0.9976$) which establishes a proportional relationship between redox current

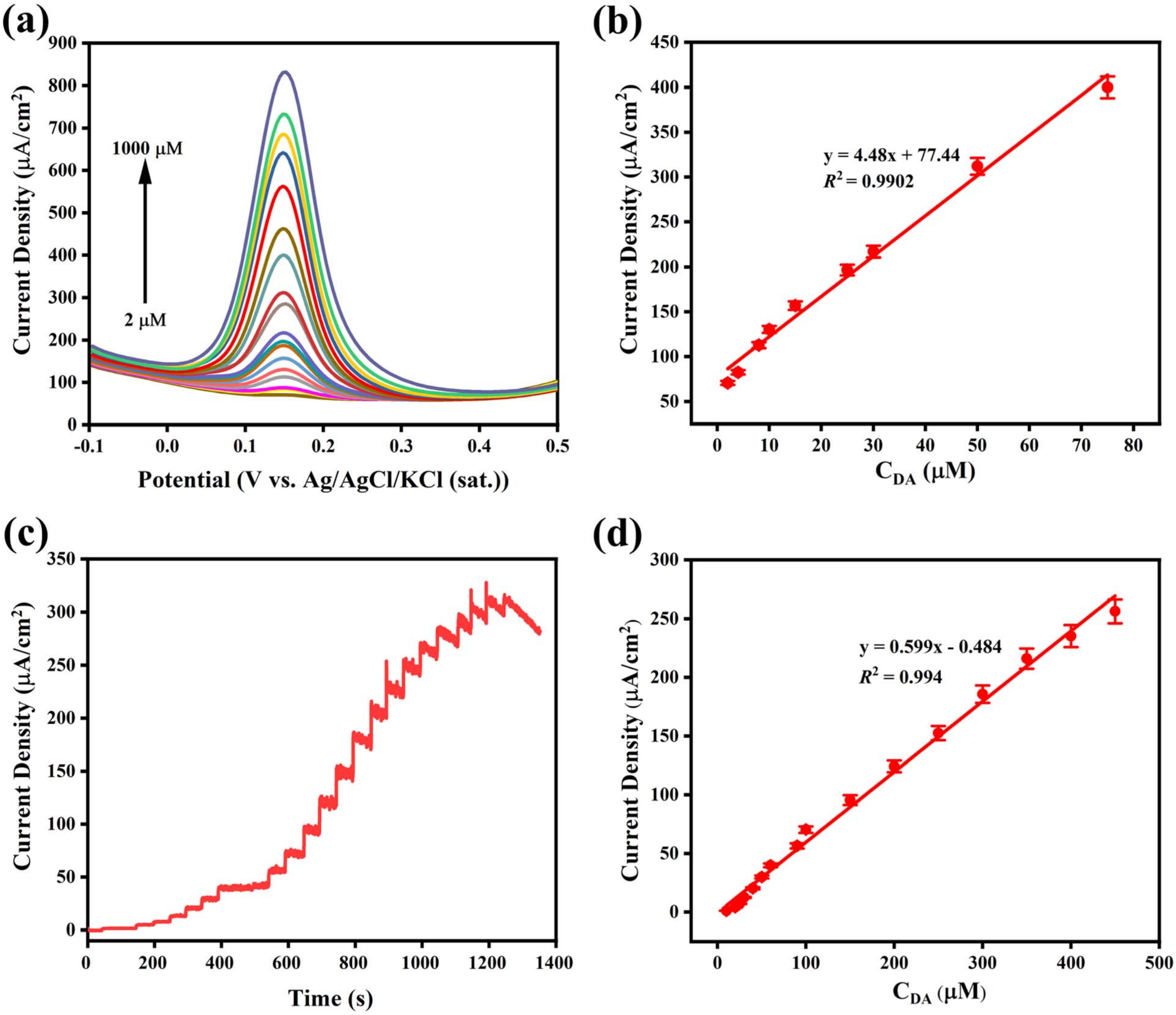

Fig. 5 (a) DPV response of rGO–Fe_3O_4/GCE in 0.1 M PBS (pH 7.4) with DA concentration ranging from 2 to 1000 μM. (b) Plot of oxidation peak current density *vs.* DA concentration within the linear range (2–75 μM). (c) Amperometric response of rGO–Fe_3O_4/GCE with subsequent addition of DA ranging from 10 to 1000 μM in 0.1 M PBS (pH 7.4) at an applied potential of 0.15 V. (d) Plot of amperometric peak current density as a function of DA concentration within the linear range (10–450 μM).

density and scan rate. Whereas, Fig. 3d presents a linear fitted plot of j_{pa} and j_{pc} as a function of $\nu^{1/2}$ with regression equation, $j_{pa} = 1384.10\nu^{1/2} - 144.82$ ($R^2 = 0.9799$) and $j_{pc} = -1157.61\nu^{1/2} + 154.34$ ($R^2 = 0.9632$), which clearly corresponds to a poor linear relationship among the axes parameters. So, it is evident that the redox reaction of DA on rGO–Fe_3O_4/GCE is adsorption controlled.

3.2.3 Effect of pH. The influence of pH on the redox reaction of DA on rGO–Fe_3O_4/GCE was studied by CV technique in 0.1 M PBS containing 100 μM DA at 50 mV s^{-1} scan rate, with varying pH from 3 to 10 as shown in Fig. 4a. A negative shift of oxidation peak potential with the increase of pH was observed, indicating the participation of protons in the electrode reaction. Additionally, Fig. 4b shows the variation of oxidation peak current density and peak potential with pH. The peak potential shows a fairly linear relationship with pH and gives a linear-fitted equation, $E_{pa} = -0.0638$ pH + 0.6902 ($R^2 = 0.9743$), where the value of the slope is 63.8 mV per pH. The slope magnitude is in proximity to the theoretical value (59 mV per pH) obtained for the involvement of same number of proton and electron according to Nernst equation.[63,64] On the other hand, j_{pa} increases almost linearly with the pH range 3–5. The rGO–Fe_3O_4 composites and individually Fe_3O_4 exhibit positive zeta potential in strongly acidic conditions but they have been found to accumulate net negative charge above pH 5.5.[65] Therefore, it can be assumed that within the pH range 3–5, protonated DA and presumably positively charged surface of rGO–Fe_3O_4 repulse each other and thus the rate of oxidation decreases. Also, DA is relatively stable at its protonated form, specifically under pH 5.4 and hence somewhat averse to electrochemical oxidation compared to neutral and basic environments.[66,67] These couple of facts may be attributed as the reasons to find lower oxidation peak current of DA on rGO–Fe_3O_4/GCE at acidic conditions. Within pH 3–5, the increase of

Table 1 Comparison of performance between several electrochemical sensors for the detection of DA[a]

Electrode	Method	Linear range (μM)	LOD (μM)	Sensitivity (μA mM^{-1})	Reference
Au–Cu_2O/rGO/GCE	DPV	10–90	3.9	—	32
Au–rGO/GCE	DPV	6.8–41	1.4	1000	74
GNPs–PANI/GCE	Amp	3–115	0.8	26.9	75
Fe_2O_3/N–rGO/GCE	Amp	0.5–340	0.49	29.60	35
GO–Fe_3O_4/GCE	DPV	1–10	0.48	277.7	33
EPPGE–SWCNT–Fe_2O_3	SWV	3.2–31.8	0.36	3440	76
Pt–rGO/GCE	DPV	10–170	0.25	39.1	77
PdNPs–rGO/GCE	LSV	1–150	0.233	207	78
rGO–Fe_3O_4/GCE	DPV	0–10	0.12	2733	79
rGO–Fe_3O_4/GCE	**Amp**	**10–450**	**0.0639 ± 0.0035**	**42.35 ± 1.77**	**This work**

[a] Amp: amperometry; EPPGE: edge-plane pyrolytic graphite electrode; GNPs: gold nanoparticles; LSV: linear sweep voltammetry; PANI: polyaniline; SWCNT: single-wall carbon nanotubes; SWV: square wave voltammetry.

current with pH may be owing to the fact that, as pH increases, proton concentration and positive surface charge of rGO–Fe_3O_4 is diminished which leads to less repulsion between like charges and thus the rate of oxidation increases. However, at pH 6, there is a decrease of current response compared to that at pH 5, which may be attributed to less efficient adsorption dynamics between negatively charged rGO–Fe_3O_4 surface and protonated DA. Repulsion between the positively charged DA molecules while competing for the available adsorption-oxidation sites of rGO–Fe_3O_4 may have contributed in this regard. Nonetheless, the highest amount of current response was found at pH 7.4, the same pH level as that of human body. The primary oxidation product of DA is DAQ which can spontaneously form polydopamine (PDA) in neutral and basic environment, thus leading to enhancement of DA oxidation rate.[68,69] At the physiological pH (7.4), DA mostly exists in a cationic form.[70] As the considered reaction is adsorption controlled at pH 7.4, cationic DA strongly adsorbs into the negatively charged surface of the rGO–Fe_3O_4 electrode at this pH, which eventually leads to a high oxidation current output. At higher alkaline conditions, DA gets significantly deprotonated,[71] leaving minimal room for opposite charge interaction and hence the oxidation current response decreases.

A plausible mechanistic pathway for DA oxidation on rGO–Fe_3O_4/GCE at the experimentally optimal pH (7.4) has been illustrated in Fig. 4c. The oxidation of DA begins with a two-electron, two-proton transfer, forming DAQ. Through 1,4-Michael addition, DAQ then cyclizes to produce 5,6-dihydroxyindoline, which is readily oxidized to indoline-5,6-dione; this intermediate then rearranges to 5,6-dihydroxyindole before undergoing further oxidation to indole-5,6-quinone.[64,72] The last two oxidative derivatives arising from this reaction sequence are capable of undergoing spontaneous polymerization, ultimately producing polydopamine.[73]

3.2.4 DPV study. The DPV response of the rGO–Fe_3O_4 electrode upon addition of 2–1000 μM DA was recorded for the detailed insight into the electroanalytical performance of the sensor, as illustrated at Fig. 5a. The DPV technique provided with an elevated current output with improved resolution. The peak potential remained consistent at 0.15 V for all concentrations which was subsequently applied as the fixed potential for all amperometric measurements (Sections 3.2.5 and 3.2.6). The oxidation peak current density (j_{pa}) increased almost linearly with the concentration of DA (C_{DA}) within 2–75 μM range (Fig. 5b). It aligns with the linear equation, $j_{pa} = 4.48C_{DA} + 77.44$, with $R^2 = 0.9902$.

3.2.5 Quantitative evaluation of DA on rGO–Fe_3O_4/GCE. Fig. 5c depicts amperometric response of rGO–Fe_3O_4/GCE to the consecutive inclusion of DA (10–1000 μM) in 0.1 M PBS of pH 7.4 at an employed potential of 0.15 V. The study shows that the current response increases linearly with 10–450 μM of DA addition. Therefore, Fig. 5d shows the plot of current density output as a function of the linear range of DA concentration, which provides with a regression equation, $j_{pa} = 0.599C_{DA} - 0.484$ ($R^2 = 0.994$). The limit of detection (LOD) of DA by rGO–Fe_3O_4/GCE was estimated by the equation, LOD $= 3s/m$, where, s is = standard deviation in current response of the blank solution and m is = slope of the calibration line. The calculated LOD value was 0.0639 μM with the sensitivity being 42.35 μA mM^{-1}. Comparison between different electrochemical sensors for detection of DA has been displayed at Table 1, which reveals that our strategy of preparing rGO–Fe_3O_4 by using e-wastes as precursors results in lower LOD, good sensitivity, and greater linear range of DA sensing. Although, there are sensors available with better performance, some of the preparation methods are complex, non-sustainable, and expensive whereas, our work involves facile, non-toxic, and cost-effective synthesis procedure which ensures proper reuse of e-waste along with consistent material performance.

3.2.6 Analysis of interference effects. Fig. 6a displays amperometric response of DA on rGO–Fe_3O_4/GCE in presence of several interfering agents at optimal potential of DA oxidation (0.15 V). A time interval of approximately 50 seconds was maintained between successive additions of two solutions. The experiment was carried out in Ar-saturated 0.1 M PBS (pH 7.4) and the concentration of each added solution was maintained at 100 μM. Initial introduction of DA in the PBS produced a significant current spike which confirms sensing of DA by the fabricated electrode. Then upon successive addition of serotonin (5-HT) and 4-nitrophenol (4-NP), any remarkable change

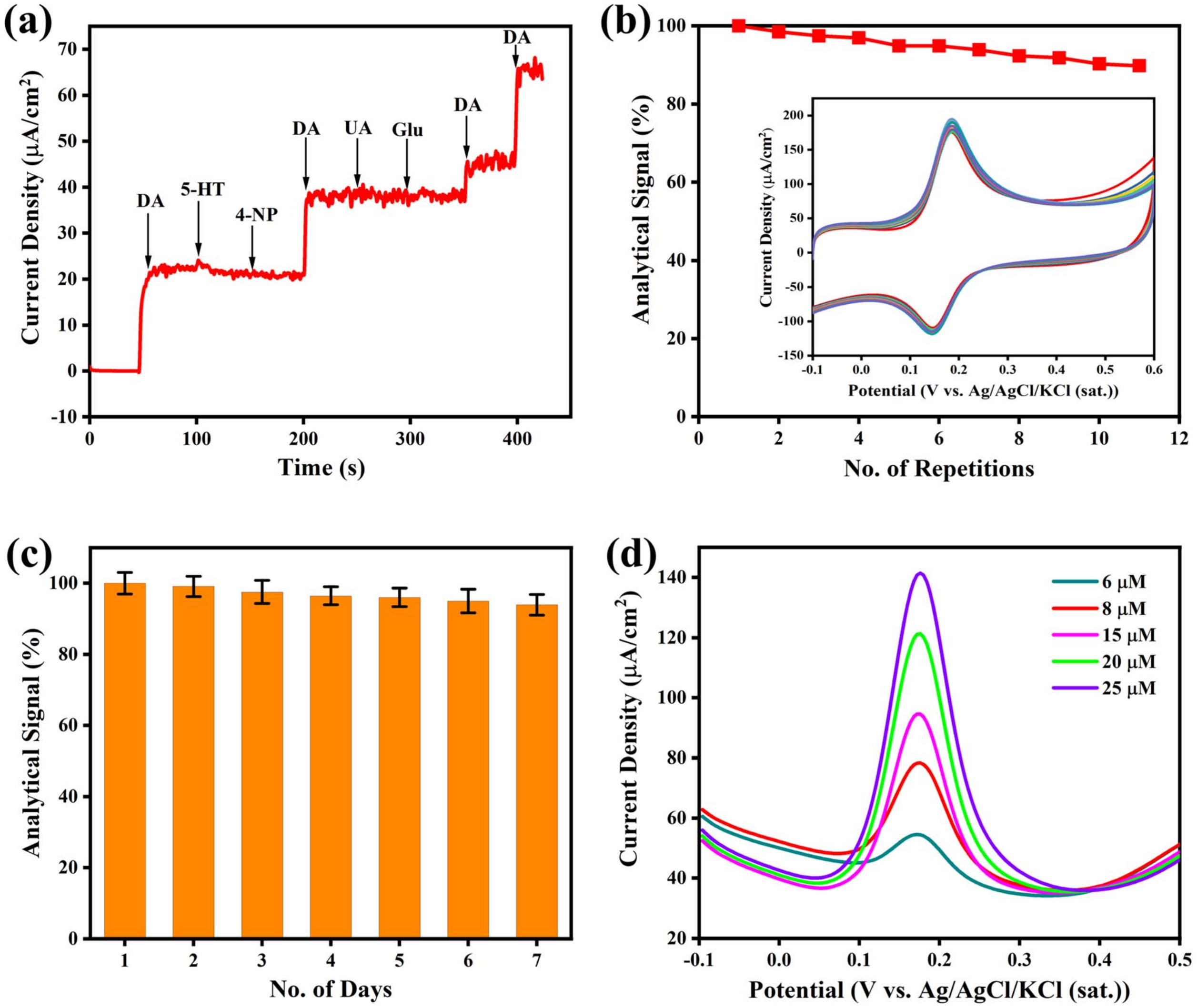

Fig. 6 (a) Amperometric response of rGO–Fe_3O_4/GCE with the successive addition of 100 µM DA, 5-HT, 4-NP, DA, Glucose, UA, DA, and DA in 0.1 M PBS of pH 7.4 at 0.15 V potential. (b) Plot of percentage of initial current response obtained from 11 consecutive CVs as a function of no. of repetition, where the inset displays the CV responses. (c) Comparison of CV responses of rGO–Fe_3O_4 modified GCE over 7 days in 0.1 M PBS (pH 7.4) containing 100 µM DA. (d) DPV responses obtained from real sample (urine) analysis.

in current response wasn't observed. Then the reintroduction of DA recorded a sharp current jump once again. Subsequent inclusion of uric acid (UA) and glucose (Glu) also didn't have any detectable response, although lastly, couple of successive addition of DA showed pronounced current output (Fig. 6a). Specifically, UA is a familiar interfering substance in the detection of DA in biological specimens and hence, being immune to disruption by UA gives rGO–Fe_3O_4/GCE a significant advantage in DA sensing.

3.2.7 Repeatability and stability.

Repeatability and stability test of rGO–Fe_3O_4/GCE was carried out employing CV technique at 50 mV s^{-1} scan rate using 100 µM DA in 0.1 M PBS (pH 7.4), which yielded significant conclusions on the operational efficiency of the electrode as a sensor. To assess repeatability, 11 consecutive CVs were taken where the final oxidation peak current was decreased by approximately 10% of the initial response (Fig. 6b). The relative standard deviation (RSD) of this experiment was estimated as 3.57%. The stability test was conducted over the course of 7 days while preserving the electrode in a refrigerator. On the final day, the electrode retained 94% of the initial current output while the experimental RSD was found to be 2.22% (Fig. 6c). Overall, rGO–Fe_3O_4 modified GCE showed decent stability and repeatability results in the detection of DA.

3.2.8 Real sample analysis.

Urine was selected as the real sample to evaluate the practical applicability of rGO–Fe_3O_4/GCE. Prior to the experiment, the urine sample was centrifuged for 10 minutes at 4000 rpm to remove cellular debris, precipitated proteins, and suspended particles. Then, 200 µL of the supernatant of the urine sample was diluted to 10 mL of 0.1 M PBS (pH 7.4) followed by sequential addition of DA at concentrations of 6, 8, 15, 20, and 25 µM. The DPV responses of the test solutions have been displayed in Fig. 6d. The recovery percentage of DA in these real samples was calculated by

Table 2 Recovery of DA from urine samples utilizing rGO–Fe_3O_4/GCE electrochemical sensor

Amount added (μM)	Amount found (μM)	Recovery (%)
6.0	6.5 ± 0.14	108.3
8.0	8.4 ± 0.19	105.0
15.0	13.9 ± 0.39	92.7
20.0	18.4 ± 0.44	92.0
25.0	24.7 ± 0.63	98.8

comparing their background-corrected current responses with the faradic current responses from standard DPV experiments at similar DA concentrations. DPV was selected for real sample analysis because it produced sharper, well-defined oxidation peaks and exhibited better reproducibility at low dopamine concentrations, enabling more reliable detection. Table 2 shows the quantitative assessment of DA in real sample solutions, where the recovery amount of DA fluctuated between 92 to 108.3%. Therefore, the rGO–Fe_3O_4/GCE exhibits satisfactory reliability for DA detection in complex biological matrix like urine and holds great potential in determining DA in biological samples.

4. Conclusions

In this study, we present a sustainable, low-cost approach for the recovery and repurposing of valuable materials from spent lithium-ion batteries and waste toner powder (WTP) and their application for electrochemical dopamine (DA) sensing. Graphite was successfully isolated from used battery anodes *via* ultrasonication, while ferric oxide was derived from WTP through high-temperature thermal decomposition. The recovered graphite was subsequently converted into graphene oxide (GO) using an improved Hummers' method, and further reduced to form rGO–Fe_3O_4 nanocomposite through chemical reduction in the presence of Fe_2O_3 precursor. This upcycling strategy not only enables efficient material recovery but also facilitates the green synthesis of functional carbon–metal oxide nanohybrid. The resulting rGO–Fe_3O_4 nanocomposite was employed as a sensing interface for the electrochemical detection of DA, demonstrating a high sensitivity of 42.35 $\mu A\ mM^{-1}$ and a low detection limit of 0.0639 μM. The developed electrode exhibited excellent selectivity for DA over common interferents, alongside good stability, repeatability, and reliable performance in real biological samples such as urine. This work exemplifies a circular materials strategy wherein, e-waste is transformed into high-performance electrochemical platforms, advancing both resource recovery and cost-effective sensor fabrication for biomedical applications.

Conflicts of interest

There are no conflicts to declare.

Data availability

Data will available on request.

Acknowledgements

The authors are grateful to the Bangladesh Council of Scientific and Industrial Research (BCSIR) for financial support (R&D ref. no. 39.02.0000.011.14.169.2023/877, date 17.09.2023) and facilities. The assistance from IERD, BCSIR, and CARS, Dhaka University to perform SEM and XRD analyses is appreciated.

References

1 I. M. S. K. Ilankoon, Y. Ghorbani, M. N. Chong, G. Herath, T. Moyo and J. Petersen, *Waste Manage.*, 2018, **82**, 258–275.

2 H. Roy, T. Rahman, M. B. Suhan, M. R. Mamun, S. Haque and M. Islam, *Heliyon*, 2022, **8**, e09802.

3 M. Abdullah, S. Adhikary, S. Bhattacharya, S. Hazra, A. Ganguly, S. Nanda and P. Rajak, *Toxicology*, 2024, **509**, 153981.

4 D. Choudhary, S. Kaithwas, Kamlesh, R. K. Sharma, A. Mishra, S. Singhai, S. Powar and A. Singh, *Environ. Technol. Innovation*, 2024, **34**, 103572.

5 S. Babar, N. Gavade, H. Shinde, A. Gore, P. Mahajan, K. H. Lee, V. Bhuse and K. Garadkar, *J. Environ. Chem. Eng.*, 2019, **7**, 103041.

6 M. Akilarasan, S. Kogularasu, S.-M. Chen, T.-W. Chen and B.-S. Lou, *RSC Adv.*, 2018, **8**, 39870–39878.

7 M. Kouser, B. Chowhan, N. Sharma and M. Gupta, *ACS Omega*, 2022, **7**, 47619–47633.

8 S. Kaipannan, K. Govindarajan, S. Sundaramoorthy and S. Marappan, *ACS Omega*, 2019, **4**, 15798–15805.

9 H. Koseki, *Procedia Eng.*, 2014, **84**, 273–279.

10 L. Li, J. B. Dunn, X. X. Zhang, L. Gaines, R. J. Chen, F. Wu and K. Amine, *J. Power Sources*, 2013, **233**, 180–189.

11 D. H. P. Kang, M. Chen and O. A. Ogunseitan, *Environ. Sci. Technol.*, 2013, **47**, 5495–5503.

12 D. Lisbona and T. Snee, *Process Saf. Environ. Prot.*, 2011, **89**, 434–442.

13 A. Zanoletti, E. Carena, C. Ferrara and E. Bontempi, *Batteries*, 2024, **10**, 38.

14 M. A. Bhakare, P. S. Dhumal, M. P. Bondarde, K. D. Lokhande and S. Some, *Colloids Surf., A*, 2024, **685**, 133196.

15 H. Zhu, Y. Zhou, S. Wang, X. Wu, J. Hou, W. Yin, K. Feng, X. Wang and J. Yang, *RSC Adv.*, 2018, **8**, 27654–27660.

16 P. Arjunan, M. Kouthaman, K. Kannan, K. Diwakar, V. Priyanka, R. Subadevi and M. Sivakumar, *J. Environ. Chem. Eng.*, 2021, **9**, 105024.

17 D. A. Bertuol, C. M. Machado, M. L. Silva, C. O. Calgaro, G. L. Dotto and E. H. Tanabe, *Waste Manage.*, 2016, **51**, 245–251.

18 S. Islam, M. H. Kabir, T. Jahan, U. S. Akhtar and S. Yasmin, *Sens. Actuators, A*, 2025, **393**, 116791.

19 M. H. Kabir, M. J. Miah, A. K. Mohiuddin, Md. S. Hossain, B. P. Upoma, M. A. A. Shaikh, M. Y. Pabel, F. Mojumder,

R. Mahmud, N. I. Tanvir and S. Yasmin, *ACS Sustainable Resour. Manage.*, 2025, **2**, 256–266.

20 J. Mohanraj, D. Durgalakshmi, S. Balakumar, P. Aruna, S. Ganesan, S. Rajendran and Mu. Naushad, *J. Water Proc. Eng.*, 2020, **34**, 101078.

21 O. Saha, M. H. Kabir, M. M. Islam, M. S. Hossain, M. S. Bashar, M. Y. Pabel and S. Yasmin, *RSC Adv.*, 2025, **15**, 41874–41885.

22 J. N. Oak, J. Oldenhof and H. H. M. Van Tol, *Eur. J. Pharmacol.*, 2000, **405**, 303–327.

23 D. D. Dougherty, A. A. Bonab, T. J. Spencer, S. L. Rauch, B. K. Madras and A. J. Fischman, *Lancet*, 1999, **354**, 2132–2133.

24 J. Segura-Aguilar, I. Paris, P. Muñoz, E. Ferrari, L. Zecca and F. A. Zucca, *J. Neurochem.*, 2014, **129**, 898–915.

25 U. H. Mitchell, J. D. Obray, E. Hunsaker, B. T. Garcia, T. J. Clarke, S. Hope and S. C. Steffensen, *Front. Neurol.*, 2018, **9**, 155.

26 J. Birtwistle and D. Baldwin, *Br. J. Nurs.*, 1998, **7**, 832–841.

27 J. Neumann, B. Hofmann, S. Dhein and U. Gergs, *Int. J. Mol. Sci.*, 2023, **24**, 5042.

28 W. Gao, L. Qi, Z. Liu, S. Majeed, S. A. Kitte and G. Xu, *Sens. Actuators, B*, 2017, **238**, 468–472.

29 N. O. A. Al-Salahi, E. Y. Hashem and D. A. Abdel-Kader, *Spectrochim. Acta, Part A*, 2022, **278**, 121278.

30 J. Wang, R. Du, W. Liu, L. Yao, F. Ding, P. Zou, Y. Wang, X. Wang, Q. Zhao and H. Rao, *Sens. Actuators, B*, 2019, **290**, 125–132.

31 S. Yasmin, D. Park and S. Jeon, *J. Electrochem. Soc.*, 2016, **163**, B491–B498.

32 T. K. Aparna, R. Sivasubramanian and M. A. Dar, *J. Alloys Compd.*, 2018, **741**, 1130–1141.

33 I. Anshori, K. Kepakisan, L. Rizalputri, R. Althof, A. Nugroho, R. Siburian and M. Handayani, *Nanocomposites*, 2022, **8**, 155–166.

34 S. Yasmin, M. S. Ahmed and S. Jeon, *J. Electrochem. Soc.*, 2015, **162**, B363.

35 Z. Yang, X. Zheng and J. Zheng, *J. Alloys Compd.*, 2017, **709**, 581–587.

36 D. M. A. Neto, L. S. da Costa, C. P. Sousa, H. Becker, P. N. S. Casciano, H. O. Nascimento, J. R. B. Neto, P. de Lima-Neto, R. F. Nascimento, J. A. C. Guedes, R. C. de Oliveira, D. Zampieri, A. N. Correia and P. B. A. Fechine, *Electrochim. Acta*, 2022, **432**, 141193.

37 W. Yang, Y. Yu, Y. Tang, K. Li, Z. Zhao, M. Li, G. Yin, H. Li and S. Sun, *Nanoscale*, 2017, **9**, 1022–1027.

38 M. Y. Pabel, S. Yasmin, M. Shaikh and M. Kabir, *Sens. Actuators, A*, 2024, **366**, 115028.

39 M. Kabir, M. Y. Pabel, N. Bristy, M. A. Salam, M. Bashar and S. Yasmin, *RSC Adv.*, 2024, **14**, 36073–36083.

40 H. Guan, Y. Chen, K. Xing and Q. Liu, *J. Food Compos. Anal.*, 2024, **136**, 106792.

41 S. Luo, M. Yang, Y. Wu, J. Li, J. Qin and F. Feng, *Micromachines*, 2022, **13**, 115.

42 D. C. Marcano, D. V. Kosynkin, J. M. Berlin, A. Sinitskii, Z. Sun, A. Slesarev, L. B. Alemany, W. Lu and J. M. Tour, *ACS Nano*, 2010, **4**, 4806–4814.

43 C. Liang, J. Song, Y. Zhang, Y. Guo, M. Deng, W. Gao and J. Zhang, *Nanoscale Res. Lett.*, 2020, **15**, 86.

44 T. F. Emiru and D. W. Ayele, *Egypt. j. basic appl. sci.*, 2017, **4**, 74–79.

45 N. T. Dipannita, S. Yasmin, M. K. Hasan, M. S. Hossain, M. A. Somapti and M. H. Kabir, *RSC Adv.*, 2025, **15**, 35219–35232.

46 D. He, Z. Peng, W. Gong, Y. Luo, P. Zhao and L. Kong, *RSC Adv.*, 2015, **5**, 11966–11972.

47 Y. Li, J. Mao, H. Xie and J. Li, *J. Mater. Cycles Waste Manag.*, 2018, **20**, 361–368.

48 F. Ghasemy-Piranloo, F. Bavarsiha and S. Dadashian, *J. Sol-Gel Sci. Technol.*, 2022, **103**, 908–920.

49 X. Pham, P. Nguyen Tan, T. Pham, T. Tran and T. Tran, *Adv. Nat. Sci. Nanosci. Nanotechnol.*, 2016, **7**, 045010.

50 M. G. Azam, M. H. Kabir, M. A. A. Shaikh, S. Ahmed, M. Mahmud and S. Yasmin, *J. Water Proc. Eng.*, 2022, **46**, 102597.

51 J. Ma, J. Lian, X. Duan, X. Liu and W. Zheng, *J. Phys. Chem. C*, 2010, **114**, 10671–10676.

52 S. S. Abouelkheir, H. A. H. Ibrahim and E. A. Beltagy, *Sci. Rep.*, 2023, **13**, 11117.

53 E. Bertolucci, A. M. R. Galletti, C. Antonetti, M. Marracci, B. Tellini, F. Piccinelli and C. Visone, in *2015 IEEE International Instrumentation and Measurement Technology Conference (I2MTC) Proceedings*, 2015, pp. 1492–1496.

54 A. Jafari, S. Farjami Shayesteh, M. Salouti and K. Boustani, *J. Magn. Magn. Mater.*, 2015, **379**, 305–312.

55 Y. He, Y. Liu, F. Guo, K. Pang, B. Fang, Y. Wang, D. Chang, Z. Xu and C. Gao, *Chin. Chem. Lett.*, 2020, **31**, 1625–1629.

56 R. Liu, X. Zhu and B. Chen, *Sci. Rep.*, 2017, **7**, 40711.

57 B. J. Venton and Q. Cao, *Analyst*, 2020, **145**, 1158–1168.

58 H. Yamada, K. Yoshii, M. Asahi, M. Chiku and Y. Kitazumi, *Electrochemistry*, 2022, **90**, 102005.

59 A. Molina, J. González, E. Laborda and R. G. Compton, *Phys. Chem. Chem. Phys.*, 2013, **15**, 2381–2388.

60 N. S. Anuar, W. J. Basirun, M. Shalauddin and S. Akhter, *RSC Adv.*, 2020, **10**, 17336–17344.

61 B. D. Bath, D. J. Michael, B. J. Trafton, J. D. Joseph, P. L. Runnels and R. M. Wightman, *Anal. Chem.*, 2000, **72**, 5994–6002.

62 J. Lang, W. Wang, Y. Zhou, D. Guo, R. Shi and N. Zhou, *Front. Chem.*, 2022, **10**, 834154.

63 N. Roy, S. Yasmin and S. Jeon, *Microchem. J.*, 2019, **153**, 104501.

64 M. Y. Pabel, M. H. Kabir, M. S. Hossain, F. Mojumder, S. Datta, M. S. Bashar and S. Yasmin, *Mater. Adv.*, 2025, **6**, 2243–2252.

65 P. K. Boruah, D. J. Borah, J. Handique, P. Sharma, P. Sengupta and M. R. Das, *J. Environ. Chem. Eng.*, 2015, **3**, 1974–1985.

66 T.-P. Chen, T. Liu, T.-L. Su and J. Liang, *Langmuir*, 2017, **33**, 5863–5871.

67 X. Du, L. Li, J. Li, C. Yang, N. Frenkel, A. Welle, S. Heissler, A. Nefedov, M. Grunze and P. A. Levkin, *Adv. Mater.*, 2014, **26**, 8029–8033.

68 S. Schindler and T. Bechtold, *J. Electroanal. Chem.*, 2019, **836**, 94–101.

69 R. P. Bacil, L. Chen, S. H. P. Serrano and R. G. Compton, *Phys. Chem. Chem. Phys.*, 2020, **22**, 607–614.

70 J. L. Berfield, L. C. Wang and M. E. A. Reith, *J. Biol. Chem.*, 1999, **274**, 4876–4882.

71 K. Jodko-Piórecka, B. Sikora, M. Kluzek, P. Przybylski and G. Litwinienko, *J. Org. Chem.*, 2022, **87**, 1791–1804.

72 N. Delmo, B. Mostafiz, A. E. Ross, J. Suni and E. Peltola, *Sens. Diagn.*, 2023, **2**, 559–581.

73 M. Bisaglia, S. Mammi and L. Bubacco, *J. Biol. Chem.*, 2007, **282**, 15597–15605.

74 C. Wang, J. Du, H. Wang, C. Zou, F. Jiang, P. Yang and Y. Du, *Sens. Actuators, B*, 2014, **204**, 302–309.

75 A.-J. Wang, J.-J. Feng, Y.-F. Li, J.-L. Xi and W.-J. Dong, *Microchim. Acta*, 2010, **171**, 431–436.

76 A. S. Adekunle, B. O. Agboola, J. Pillay and K. I. Ozoemena, *Sens. Actuators, B*, 2010, **148**, 93–102.

77 T.-Q. Xu, Q.-L. Zhang, J.-N. Zheng, Z.-Y. Lv, J. Wei, A.-J. Wang and J.-J. Feng, *Electrochim. Acta*, 2014, **115**, 109–115.

78 S. Palanisamy, S. Ku and S.-M. Chen, *Microchim. Acta*, 2013, **180**, 1037–1042.

79 T. Peik-See, A. Pandikumar, H. Nay-Ming, L. Hong-Ngee and Y. Sulaiman, *Sensors*, 2014, **14**, 15227–15243.